



Defect engineering of nanostructured ZnSnO₃ for conductometric room temperature CO₂ sensors

Chao Zhang^{a,*}, Kewei Liu^a, Zichen Zheng^a, Marc Debligny^b

^a College of Mechanical Engineering, Yangzhou University, Yangzhou 225127, Jiangsu, PR China

^b Service de Science des Matériaux, Faculté Polytechnique, Université de Mons, Mons 7000, Belgium

ARTICLE INFO

Keywords:

Oxygen vacancy
Gas sensor
Hydrogen reduction
Light activation
DFT calculation

ABSTRACT

Slow response/recovery kinetics and high limit of detection (LOD) are crucial challenges for practical room-temperature carbon dioxide (CO₂) gas sensor platforms. Herein, visible light-excited ZnSnO₃ three-dimensional nanostructures are utilized for highly sensitive and selective detection of CO₂. The sensing performance reveals that fine-controlled oxygen vacancy (O_v) and highly-active electron transition of defect-rich nanomaterials are obtained via modulating the hydrogen treatment duration, conducive to the prominently enhanced ppm-level CO₂ response with low LOD (3.05 ppm), ultrafast response time (16.814 s) and improved stability (14.658 ± 2.339 @ 400 ppm for 14 days) among all the reported ternary metal oxide semiconductor (TMOS)-based gas sensors. The photophysical enhancement mechanism of analyte is discussed in detail by combining experimental and theoretical investigation through the effect of photoexcitation on both adsorbed CO₂ molecules and sensing materials, the role of pre-adsorbed oxygen for regulating targeted gas interaction, the changes of electronic transition in the bandgap, the impact of in-plane O_v and bridging O_v on CO₂ sensing, and the function of O_v for modifying the coordination sites and geometry of metal cations at the surface. From a broader perspective, the fabricated sensor provides a remarkably facile and effective technique for rapid and repeatable CO₂ monitoring.

1. Introduction

Monitoring the content of CO₂ in the atmosphere and the workplace has been under constant research for CO₂ acting as the root of global warming [1]. The authoritative report indicated that the measured atmospheric CO₂ concentration, which was around 315 ppm in the late 1950 s, reached an all-time high of 422.06 ppm on the 26th of April 2022. Besides, the rate of concentration changes has been more than 100 times faster than prehistoric humans, leaving many ecosystems unable to adapt [2,3]. Carbon neutralization has been a huge talking point for a global joint response to climate change. The data suggests that the huge effect on the climate system caused by the small feedback resulting from the increase of CO₂ concentration must be brought to the forefront [4,5]. The potential problem that CO₂ poses a serious threat to human health, such as fatigue, headache, anxiety, loss of energy, jelly legs, lung ventilation problems, etc., when the concentration exceeds the maximum safe level of 5000 ppm should not be ignored [6]. The LOD of CO₂ reaching 300 ppm can realize the research of respiration of Mycobacterium tuberculosis to provide a basis for the diagnosis of

tuberculosis. Besides, much progress has been made so far in CO₂ detection for food packages, grain mildew, carbonated drinks, wine production, fire extinguishers, etc. [7–9]. Thus, CO₂ gas detection enables many applications and has tremendous potential for hopefully environmental and social issues [10–13].

The selection of sensing materials with high sensitivity to CO₂ at low or room temperature (RT) is one of the priority things for commercializing sensors. As CO₂ is a non-polar molecule established by polar bonds, it is difficult to break through the energy barrier by surface interaction to modulate the energy band structure and carrier concentration, which is an urgent problem to be addressed. Most CO₂ gas sensors reported including binary and ternary metal oxide semiconductor-based suffered from drawbacks of high operation temperature (usually above 200 °C), complex preparation procedure, poor response and high tested concentration (over thousands of ppm), setting strict limits on their popularization [14–21]. The state-of-the-art CO₂ gas sensors based on TMOS was provided in Fig. 1a (details given in Table S1). There is an enormous amount of literature and data exploring the application of ZnSnO₃ to detect volatile organic compounds [22–25], such as HCHO [26], acetone

* Correspondence to: College of Mechanical Engineering, Yangzhou University, Huayang West Road 196, Yangzhou 225127, Jiangsu, PR China.
E-mail address: zhangc@yzu.edu.cn (C. Zhang).

[27], ethanol [28], toluene [24], triethylamine [25], n-butanol [29], n-propanol [30], 1-octen-3-ol [31] and toxic harmful gas, such as H_2S [24,32], NO_2 [33], CO [34]. Based on our previous research, $ZnSnO_3$ has also been demonstrated as a promising candidate for RT CO_2 detection [35]. In addition, various sensitization methods including doping [36], loading [37], structure regulation [35,38,39], etc., have been investigated deeply. Wang et al. utilized KOH solution for alkali etching to synthesize $ZnSnO_3$ with controlled concentration of O_V for H_2S gas sensing [40]. And beyond that, O_V -tuned $ZnSnO_3$ with improved interfacial electron transfer is rarely reported.

Hydrogen (H_2) thermal treatment is commonly used to introduce O_V through the interaction between hydrogen atoms and lattice oxygen (O_L), accompanied by the generation and release of H_2O molecules [41, 42]. Besides, the O element in materials with a molten state is usually lower than the stoichiometric ratio, of which the evaporation rate is generally faster than that of the metal atoms. Therefore, abundant O_V will be formed due to the unbalanced stoichiometric ratio maintained in the materials after rapid cooling. Recently, this method of introducing O_V has found an increasingly wide utilization in ZnO materials, but related application on $ZnSnO_3$ materials has not been reported [43–47].

In this paper, we synthesized the $ZnSnO_3$ nanocubes ($ZnSnO_3$ -NCs) with rambutan morphology after various H_2 treatment times, contributing to the enhanced sensing performance based on tuned O_V concentrations with a combination of low LOD (3.05 ppm), high response (~ 15.374), short response/recovery time (τ_{res}/τ_{rec}) (~ 16.814 s / ~ 187.593 s) for 400 ppm CO_2 . In particular, the sensitivity toward CO_2 of the fabricated gas sensor reached 3.594%/ppm under purple light illumination (395–400 nm), which is the highest among the prevailing TMOS-based gas sensors so far. As a major hurdle for room-temperature CO_2 gas sensors, the slow response and recovery kinetics were improved through light illumination and O_V introduction. Moreover, density functional theory (DFT) calculation was studied to elaborate the enhanced sensing mechanism.

2. Experimental

2.1. Synthesis of defect-rich $ZnSnO_3$

$ZnSnO_3$ -NCs with tuned O_V were synthesized through a simple two-step strategy as given in Fig. S1. First, $ZnSnO_3$ was obtained by a facile hydrothermal method as reported in our previous research [39]. The white powders of this step were defined as H-0. Second, the synthesized $ZnSnO_3$ -NCs were placed in crucibles and were heated in a tubular furnace with H_2 passing through at 500 °C for 0.5 h, 1 h, 3 h, and 5 h, respectively with the heating rate of 10 °C/min, mentioned as H-0.5, H-1, H-3 and H-5 throughout the entire article.

2.2. Gas sensor fabrication and measurements

Initially, the as-obtained $ZnSnO_3$ powder (~ 2 mg) was mixed with an appropriate amount of deionized water (~ 1 mL) by using a mortar fully grounded for 5 min until a thick paste formed. Then, it was coated onto an alumina substrate (6 *30 mm) with Pt electrode by a droplet coating method. The gas sensors were obtained after drying at RT. The gas-sensing test was performed via a four-channel gas sensing testing instrument (Wuhan Huachuang Ruike Technology Co., Ltd.), which measures electrical resistance signals of the corresponding channel in high pure air and target gas, and outputs the variation rule of the resistance with time. All the experiments without additional humidification were carried out at RT (~ 25 °C) and 10% relative humidity (RH). The response of n-type $ZnSnO_3$ is defined as R_a/R_g , in which R_a refers to the stable resistance in the air and R_g refers to the stable resistance in CO_2 . The τ_{res}/τ_{rec} is taken from the time when the total resistance change reaches 90%.

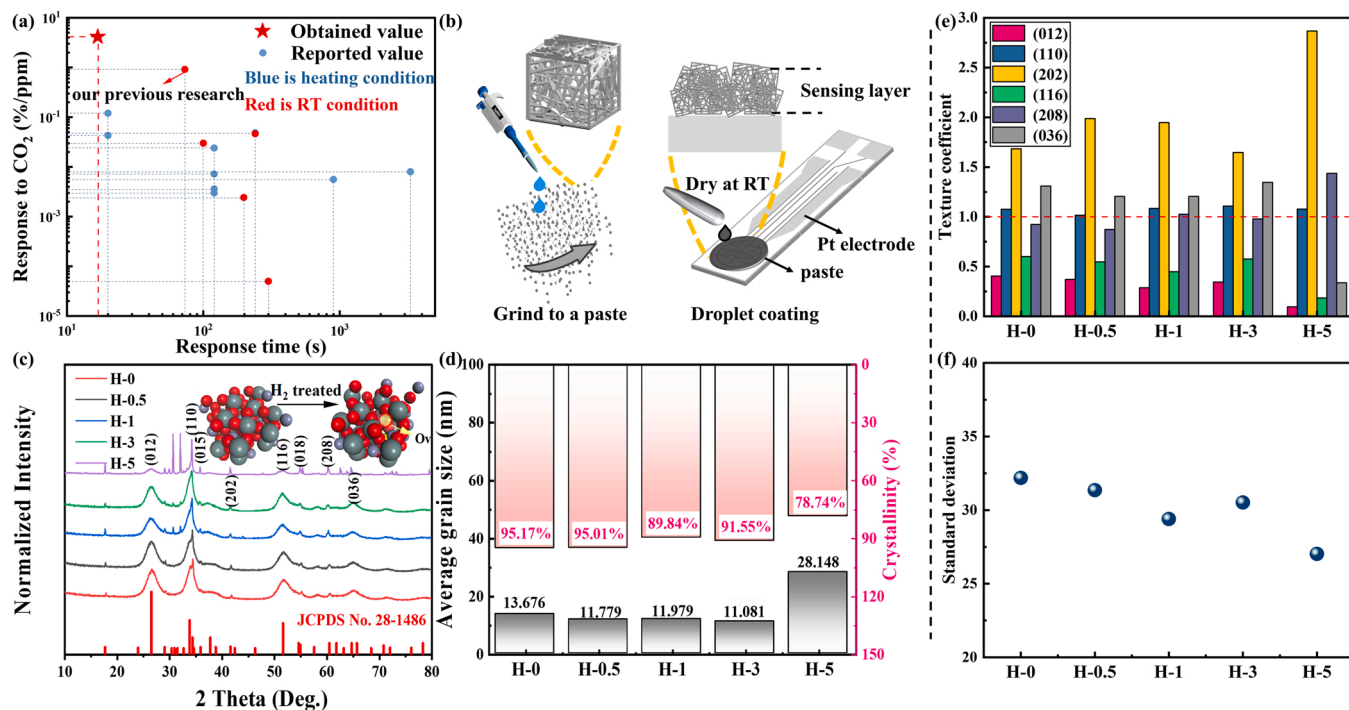


Fig. 1. (a) Comparison of as-synthesized $ZnSnO_3$ with 14 state-of-the-art CO_2 gas sensors based on TMOS in the literature in terms of the response (%/ppm) and τ_{res} . (b) Schematic diagram for the fabrication of $ZnSnO_3$ based gas sensor via droplet coating. (c) XRD spectra of all samples and crystal schematic structure of $ZnSnO_3$. (d) Calculated grain size and crystallinity. (e) Texture coefficient values. (f) Variation of standard deviation with H_2 treatment times.

3. Result and discussion

3.1. Characterization of ZnSnO₃

To characterize the crystal structure of ZnSnO₃-NCs, X-ray diffraction (XRD) patterns measured through a Cu-K α anode source depicted in Fig. 1c demonstrated that the single-phase orthorhombic perovskite structures (Pnma) were formed in all samples during H₂ treatment time of 0–5 h, and the whole diffraction peaks can be classified as the standard card (JCPDS: 28–1486), which was further confirmed by the matching of the calculated and standard *d*-spacing provided in Table S2. Compared with bulk materials, H-0, 0.5, 1 and 3 had fairly widened peaks attributing to the refined crystallite sizes as calculated via Scherrer equation in Fig. 1d, which was actuated by the enhancement of free energy of nanostructure accompanied with the increase in the total area of grain boundary and potential barrier among nanograins. Notably, the crystallinity did not present a common increase with the prolongation of thermal treatment time, probably resulting from the rapid heating rate and dramatically short heating duration in the synthesis process [48]. Besides, more defects formed in samples affected their crystallization degree and contributed to the weakened intensity of some diffraction peaks. Thus, H-3 sample presented the lowest average crystalline size and relatively high crystallinity, making it more likely to possess excellent gas sensing properties in the subsequent CO₂ sensing test. One significant difference was that the intensity of (110) peak, which was the strongest peak observed in Fig. 1c, decreased when the H₂ treatment time extended to 5 h. To figure out the reason, the texture coefficient (TC) value was used for investigating the preferred orientation (Fig. 1e). The variation of reduction time caused re-orientation effect, manifesting that (202) got preferential growth and was cumulatively exposed on the surface. TC values of (110) and (036) reached maximum of 1.108 and 1.346 for H-3 sample, and the extension of reduction duration resulted in a change in preferred orientation to (208) plane for H-5 sample. Fig. 1f showed that a small change appeared in the standard deviation of all samples, signifying that H₂ treatment brought about the heterogeneous nucleation [49]. All the calculations were defined as Equation (S1)–(S5).

As seen in Fig. 2a–d, the obtained samples were composed of rambutan-like shells with rough porous surfaces made of dense nanorods and uniform size. The wall thicknesses were extremely thin equivalent to 30–50 nm, and the edge length of a single nanocube was

around 0.77–1.07 μm . TEM results were utilized to show further insight into crystalline details. As evident in Fig. 2e–h, the clearly visible crystal lattice fringes and concentric rings comprising of abundant bright spots demonstrate that the synthesized samples are highly crystallized and possess typical polycrystalline nature. It is known to all that O_V are easily formed in grain-boundaries, contributing to the establishment of grain-boundaries state. The spots of H-3 were more distinct than those of H-0, indicating H-3 had higher crystallinity (in line with Fig. 1d). The lattice fringes were 0.336 nm, 0.264 nm and 0.177 nm assigned to interplanar spacing of (012), (110) and (116) planes, substantiating well with XRD results and the calculated *d*-spacing given in Table S2. The easily discernible grain boundary is conducive to the formation of O_Vs, which also implies a less degree of agglomeration for samples.

The surface elemental compositions of as-synthesized samples were elucidated through X-ray photoelectron spectra (XPS) as shown in Fig. 3. Notably, peaks of Zn 2p and Sn 3d of all the H₂ treated samples are shifted towards lower binding energy due to the existence of O_V and phase transformation from Sn⁴⁺ to Sn²⁺, and more shifts are found for H-1 and H-3 samples, demonstrating that rich O_V has been formed in both of them [47,50]. Fig. 3c displays the deconvoluted curves of Sn 3d resolved into three spin-orbit doublets, in which the mixture of two Sn oxidation states may result from the removal of O from the surface of the H₂ treated samples to partially reduce the Sn⁴⁺. In Fig. 3d, the O 1s spectra of all samples are deconvoluted into three peaks located at approximately 529.75 eV, 530.55 eV, and 531.44 eV via Gaussian fitting, which is attributed to O_L, O_V and chemisorbed oxygen (O_C), respectively. Fitted peak area ratios of O_V and O_C were increased after H₂ thermal treatment, indicating that the O_V was successfully formed and the concentration of O_V grew gradually, which is considered to be a key factor in enhancing the sensing performance. Besides, the generation of O_C is mainly associated with the O₂ and H₂O adsorbed on the surface of ZnSnO₃ powders, and H₂O molecules tend to be produced through the interaction between hydrogen atoms and O_L. The electron paramagnetic resonance (EPR) analysis shown in Fig. 3c displays a spectrum composed of a strong isotropic signal situating very close to *g* = 2.003, derived from a medium rich in surface defects considered as positively charged O_V, which represents electrons trapped in an O_V [51]. The sharper signals of H-1 and H-3 are obviously visible, which is assigned to the higher content of paramagnetic O_Vs. To further study the defects in as-synthesized samples, Fig. 3f exhibits the Photoluminescence (PL) emission spectra with wavelengths ranging from 450

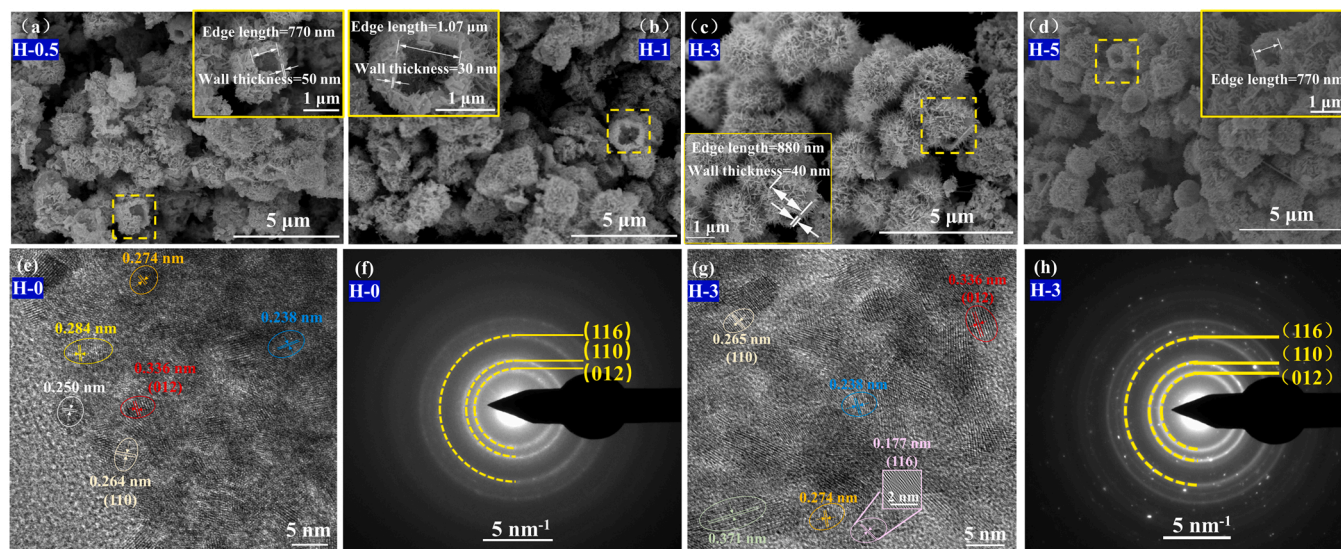


Fig. 2. FE-SEM images of (a) H-0.5, (b) H-1, (c) H-3, (d) H-5. Inset: the magnified SEM images of them. High-resolution TEM images of (e) H-0 and (g) H-3. The crystallites in the images are color-coded according to their lattice fringes. SAED analysis of (f) H-0 and (h) H-3 by drop-casting suspension on TEM grids and drying in air.

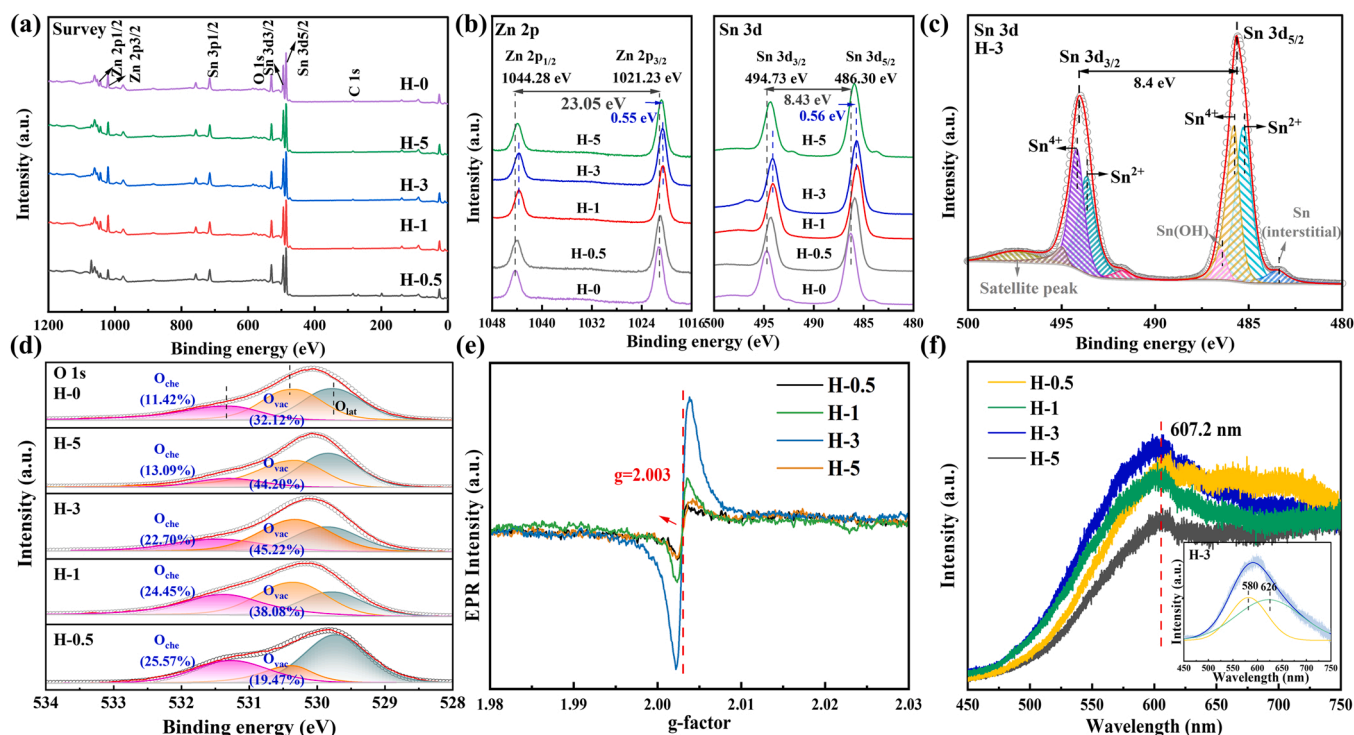


Fig. 3. (a) Full XPS spectra, (b) Zn 2p and Sn 3d spectra, and (d) O 1s spectra of all samples. (c) Deconvoluted Sn 3d spectra of H-3. (e) EPR spectra and (f) PL spectra of H-(0.5, 1, 3, 5). Inset: The Gaussian curve fitting for the PL spectra of H-3.

to 750 nm. The highest intensity of H-3 demonstrates the high O_V concentration. It is shown by comparison to the results reported in the literature that luminescence peaks of all samples experience significant redshift due to the presence of other defects such as tin vacancies [40]. The fitted peak centered at ~ 580 nm is attributed to the O_V , and the other appears at ~ 626 nm is ascribed to tin vacancies.

UV-vis absorption spectra displayed in Fig. 4a exhibited that with the introduction of O_V , samples presented absorption of the entire UV-vis range, stretching to the infrared region. The calculated forbidden bandwidths of H-0.5, H-1, H-3, and H-5 were 2.66 eV, 2.58 eV, 2.12 eV and 2.32 eV depending on Tauc plots obtained via Equation (S6), which were significantly less than that of H-0 (3.52 eV), indicating that the existence of O_V promotes the hybridization occurring between new

donor level and upwardly moving valence band (VB). The porosities of H_2 treated samples were studied through N_2 physisorption after supercritical desiccation as evident in Fig. 4b, which emerged type-IV isotherm, representing that they all possessed the characteristics of mesoporous. The specific surface areas of four samples were similar due to the presence of voids among a tightly-stacked pile of nanorods/nanosheets with hollow space inside. The pore size distribution curves indicated that the pore diameters of H-1 and H-5 were more uniform with narrower peak widths. The gas diffusion in H-3 sample was supposed to be the easiest because of the largest BET surface area ($107.017 \text{ m}^2/\text{g}$), pore size (3.716 nm) and total pore volume ($0.222 \text{ cm}^3/\text{g}$) (Table S4).

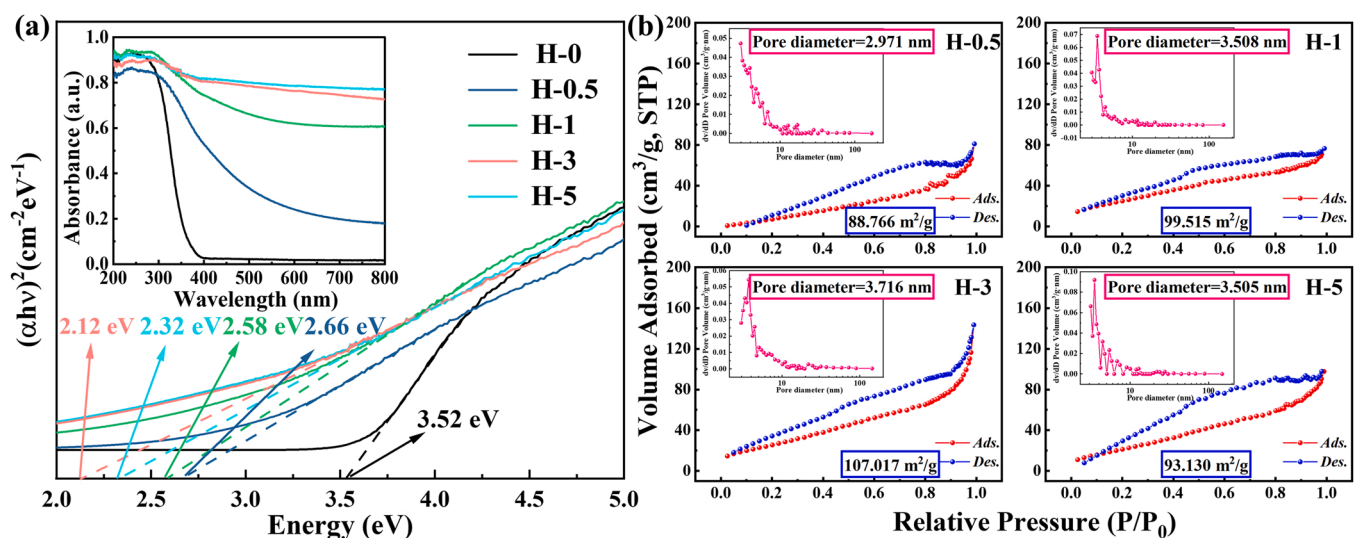


Fig. 4. (a) Tauc plots of all samples. Inset: UV-vis absorption spectra. (b) Nitrogen adsorption-desorption isotherms. Inset: Barrett-Joyner-Halenda pore-size distributions of H-(0.5, 1, 3, 5) through fitting the desorption branch of isotherms.

3.2. Gas sensing performances

The CO₂ gas sensing tests were conducted through a homebuilt apparatus (Fig. S2). Fig. 5 depicted the sensing characteristics of pristine ZnSnO₃-NCs and ZnSnO₃-NCs with a certain concentration of O_V (O_V-ZnSnO₃) to diverse CO₂ concentrations from 400 to 50 ppm in air at RT. CO₂ exhibited reductive properties, resulting in a drop in resistance immediately after its contact with sensing layers and a rapid recovery after CO₂ removal (Fig. S10a-c). Dynamic response-recovery curves of H-1 sensor towards CO₂ under different LED lights with the constant intensity identical at 1.0 mW/cm² were provided in Fig. 5a. Purple light was found to be the most effective in accelerating the response of H-1 sensor with the lowest LOD and the highest response values (R) (τ_{res} =18.21 s, LOD=3.05 ppm, R=10.73 for 400 ppm CO₂). No evident regularity was discovered when H-1 sensor operated in dark and under blue light (460–465 nm). As the wavelength shortened further, the gas sensing performance experienced significant improvement for increased photo energy. The transient response curves of gas sensor based on O_V-ZnSnO₃ depicted that H-3 sensor presented excellent sensing appearances with almost full-scale responses, of which the response values toward 400 and 50 ppm CO₂ were 3.1 and 2.5 times those of H-0 sensor (Fig. 5b). The optimal response of H-3 was caused by the generation of abundant electrons in the conduction band (CB) for its highest O_V concentration, which increased the chemisorbed O₂ molecules on the

oxygen vacant surface compared with stoichiometric one. All sensors showed linearly increased response with an elevation in CO₂ concentration ranging from 50 ppm to 400 ppm without saturation. The calculated LOD of H-3 sensor reached 3.51 ppm. Fig. 5c displayed that the τ_{res} and τ_{rec} were shortened and prolonged with the increase of H₂ treatment time respectively, the comparatively long τ_{rec} of H-3 sensor could be attributed to the sluggish desorption of the adsorbed CO₂ molecules from the mesoporous structure, tally with the BET results. In addition, compared with the 14 state-of-the-art CO₂ gas sensors based on TMOS in Fig. 1a, H-3 sensor is strikingly the best performer with excellent response and fast τ_{res} , proving that purple light excitation is a feasible and remarkably effective strategy for enhancing the overall performance of O_V-ZnSnO₃ based sensor towards CO₂. The apparent changes in reference resistance under different wavelengths of light illumination were discovered in Fig. S12a, which experienced sustained fall as the light wavelength continued to decrease for more electron-hole pairs generating on surface. The maximum resistance variation of 23 G Ω as the light changed from lower energy green (520–525 nm) to higher energy blue (460–465 nm) for the blue light surpassing the calculated forbidden bandwidth of H-1 sample (481 nm), caused by the photoexcitation generating abundant electron-hole pairs as additional charge carriers, which in turn reduced the electrical resistance macroscopically. Besides, whether the photoexcitation of ZnSnO₃ based sensors was the main factor of the light-excited CO₂ sensing performance was also

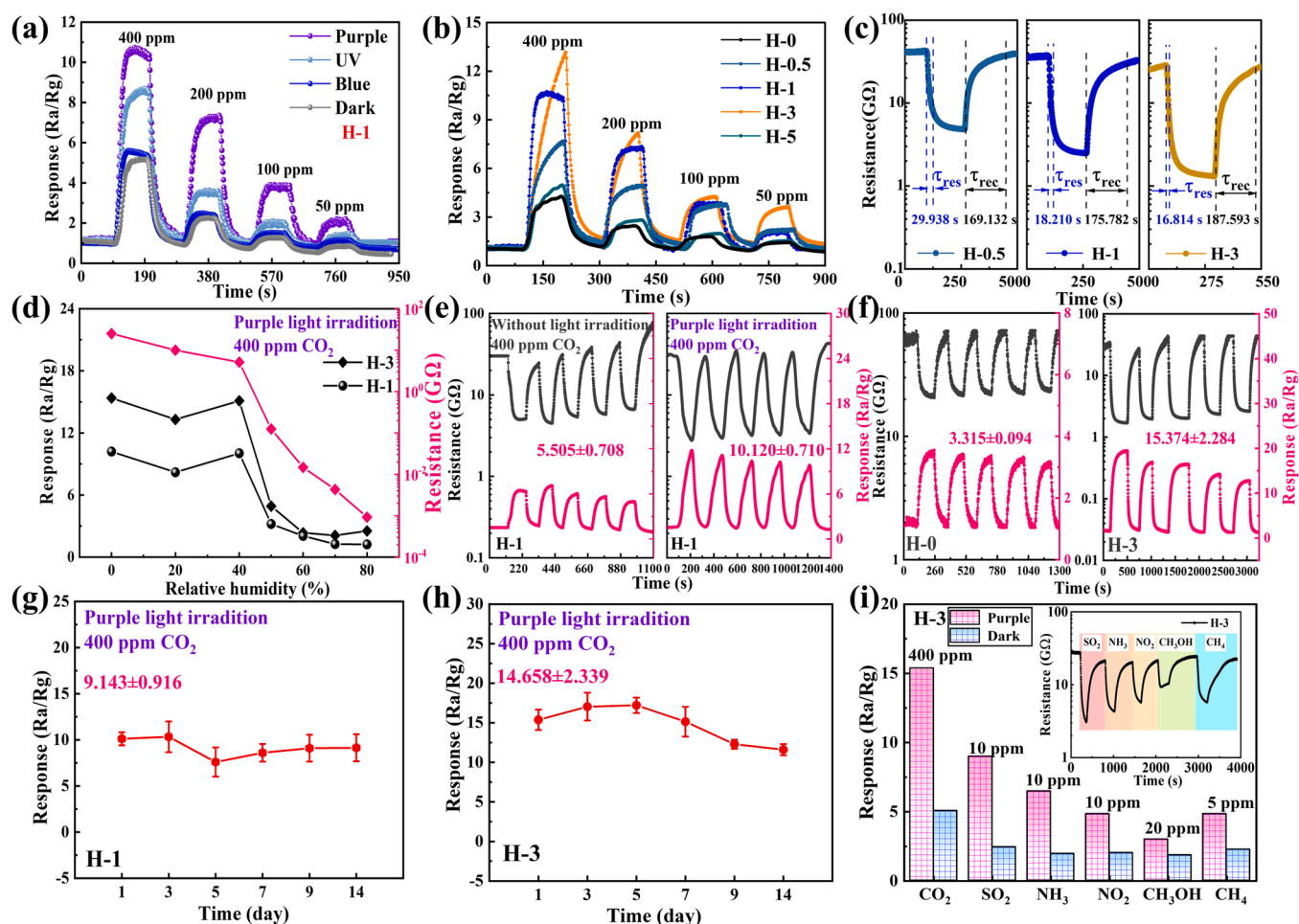


Fig. 5. (a) Response-recovery curves of H-1 sensor to 400–50 ppm CO₂ under various light irradiation conditions. (b) Response-recovery curves of all sensors exposed to 400–50 ppm CO₂ at purple light irradiation. (c) τ_{res} and τ_{rec} of H-(0.5, 1, and 3) towards 400 ppm CO₂. (d) Gas response of H-1 and H-3 and reference resistance of H-3 under different RH. Reproducibility of (e) H-1 sensor exposed to 400 ppm CO₂ (5 cycles) under dark condition (left) and purple light irradiation (right) and (f) H-3 (left) and H-3 (right) sensors to 400 ppm CO₂ (5 cycles) under purple light irradiation. Stability (within 14 days) of the (g) H-1 sensor and (h) H-3 sensor to 400 ppm CO₂ under purple light irradiation. (i) Selectivity to various gases under purple light irradiation (pink) and dark condition (blue). Inset: the dynamic resistance curves for detecting interference gases.

studied based on the temperature variation inside the chamber. As seen in Fig. S12b, switching purple light caused an observable temperature change when the CO₂ concentration remained consistent, which did not change as the constant CO₂ concentration increased to 400 ppm. In addition, the temperature of chamber did not vary when CO₂ was introduced under the condition of constant light irradiation. Therefore, the photoexcitation of sensing layer was responsible for the enhanced sensing performance.

The effect of RH is fundamental to investigate the discrimination ability of the semiconductor gas sensors (Fig. 5d and S13). The response first increased from 20% to 40% RH and then decreased, which can be explained as follows. First, H₂O dissociates and the neutral H atom reacts with the O_L, producing OH⁺ hydroxyl group with low electron affinity which will ionize and donate electrons to the CB. Second, zinc and tin bind to the produced hydroxyl group followed by electron ionization to create O_V, thus enriching the free carrier concentration and further increasing the O_V, which results in the expedited adsorption of oxygen species on the surface. The total concentration of adsorption sites (S_t) can be described as Eq. (1).

$$S_t = S_{t0} + k_0 p_{H_2O} \quad (1)$$

Where S_{t0} represents the quantity of adsorption sites without additional humidity and p_{H₂O} represents the partial pressure of water vapor (proportional to the RH). Thus, the response experienced a slight downshift when the RH rose to 20%, resulting from the surface covered with less hydroxyl groups and oxygen species. When RH reached 40%, the coverage rate of hydroxyl groups and oxygen species increased. Nevertheless, when RH exceeded 40%, a large hydroxyl groups overlay limited the oxygen species coverage, contributing to the weakness in response. The coefficient of variation (CV) of H-1 and H-3 were calculated to be 74.1% and 73.4% when changing RH from 20% to 80% through Equation (S9), which demonstrated that H-3 sensor with a lower CV value possessing the better anti-interference performance [52]. Besides, it can be calculated that 1% RH causes a 16.055% response change while 1 ppm CO₂ contributes to a 3.373% response change. That is, 1% RH change has the same effect on the sensor signal as 4.76 ppm CO₂ concentration change.

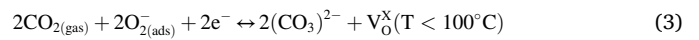
The purple light-excited H-1 sensor possessed high stability during 400 ppm CO₂ exposure/removal cycles (Fig. 5e). The response value reached 10.120 with a standard deviation of 0.710 after 5-cycle test, 83.83% higher than its counterpart without light illumination. Fig. 5 f exhibited the 5 reversible cycles of H-0 and H-3 by exposing both under purple light, the response of H-0 and H-3 stayed constant at 3.315 ± 0.094 and 15.374 ± 2.284, which means that the introduction of a moderate amount of O_V increases the response value by 363.8%. Besides, Fig. 5 g and 5 h showed that the sensor responses of H-1 and H-3 fluctuated around 9.143 and 14.658 during 14-day-long stability tests of 10 cycles per day, indicating the strong adhesion of samples to the substrate and prominent stability of sensors. The dynamic resistance curves of H-1 and H-3 on the day of the tests were provided in Fig.S14 and S15.

Fig. 5i illustrated the response of H-3 sensor towards 5 potential interfering gases in dark and under purple light irradiation at RT. The relatively low concentrations for interference gases were utilized due to their low contents compared to CO₂ in the actual application environment. The detection results showed that the purple light illumination significantly improved the selectivity to CO₂ (optimized by 26.337%, 87.942% and 42.157% for SO₂, CH₃OH and CH₄, respectively). One of the reasons may be that the aerodynamic equivalent diameter of CO₂ (3.3 Å) is relatively small compared to those of other detected gases (4.1 Å for SO₂, 4.7 Å for CH₃OH and 3.8 Å for CH₄), enabling CO₂ to diffuse into the sensing medium more easily.

3.3. Gas sensing mechanism

The sensing mechanism based on characterization, sensing performance and theoretical simulation of O_V-ZnSnO₃ has been analyzed as follows.

The variational resistance of synthesized samples depends on the regulation of the depletion region on the sensing layer surface and between the nanograins as evident in Fig. 6a. Once the sensing layer encounters high pure air, the formed O_{2(ads)}⁻ will boost the base resistance of n-type ZnSnO₃ and thicken the surface depletion layer through capturing the electrons from CB (Eq. (2)). The contact of adjacent nanograin causes the combination of depletion layer and formation of Schottky barrier for weakening the conductivity of the sensor. Subsequently, when CO₂ bubbled into gas chamber, O_{2(ads)}⁻ will react with CO₂ to generate metastable carbon tetroxide ((CO₃)²⁻) within a very short interval of time and neutral O_V (V_O^x), and then the dissociation of (CO₃)²⁻ and ionization of V_O^x will start with electrons release, contributing to the downtrend in resistance (Eqs. (3)–(6)) [21,53,54].



Where V_O^x is singly charged O_V and V_O^{**} is doubly charged O_V. V_O^{**} will be formed when a hole is trapped at V_O^x center. When CO₂ is removed and high pure air blows in, the O_{2(ads)}⁻ appears to rejuvenate O_V-ZnSnO₃ surface. The photogenerated oxygen ions (O_{2(hv)}⁻) are more active than O_{2(ads)}⁻, thus O_V-ZnSnO₃ possessed relatively short τ_{res}. However, the bond energies of O-O and C-O are 498 and 799 kJ/mol respectively, which makes gas desorption energy (E_{des}) increase and thereby hinders the desorption process and prolongs the τ_{rec} based on Eq. (7).

$$\tau_{rec} = \tau_0 \exp(E_{des}/kT) \quad (7)$$

Where k is Boltzmann constant and T is absolute temperature. In order to investigate the role of pre-adsorbed oxygen for regulating CO₂ interaction, gas sensing performance of H-3 under nitrogen (N₂) atmosphere has been studied as shown in Fig. 6b and Fig. S16. Reference resistance showed an obvious downward trend for the decreased density of pre-adsorbed oxygen species bound to the sensing materials' surface and more free carriers located in the CB. Moreover, the sensor detected under N₂ atmosphere displayed significantly different responses in shape and magnitude to that observed under a high pure air atmosphere, indicating that the sensing mechanism necessarily relied on pre-adsorbed oxygen species on the surface. Besides, the correlation effect between crystalline sizes and crystallinity has a noteworthy impact on gas sensing performance. The response and recovery processes occur simultaneously in nature. As depicted in Fig. 1d, H-0 and H-0.5 possessed higher crystallinity but poorer response, which attributes to the increased crystalline sizes offsetting the enhancement because of higher crystallinity, resulting in O₂ and CO₂ easily diffusing along grain boundaries accompanied by a decreased response.

The introduction of O_V enhances the electronic transition in the band gap. In n-type ZnSnO₃, the fully ionized O_V will release electrons into the CB as illustrated in Eq. (8) [55].



The generated O_V acts as bulk donor with a defect state below the bottom of CB, and the distance between them is equivalent to defect

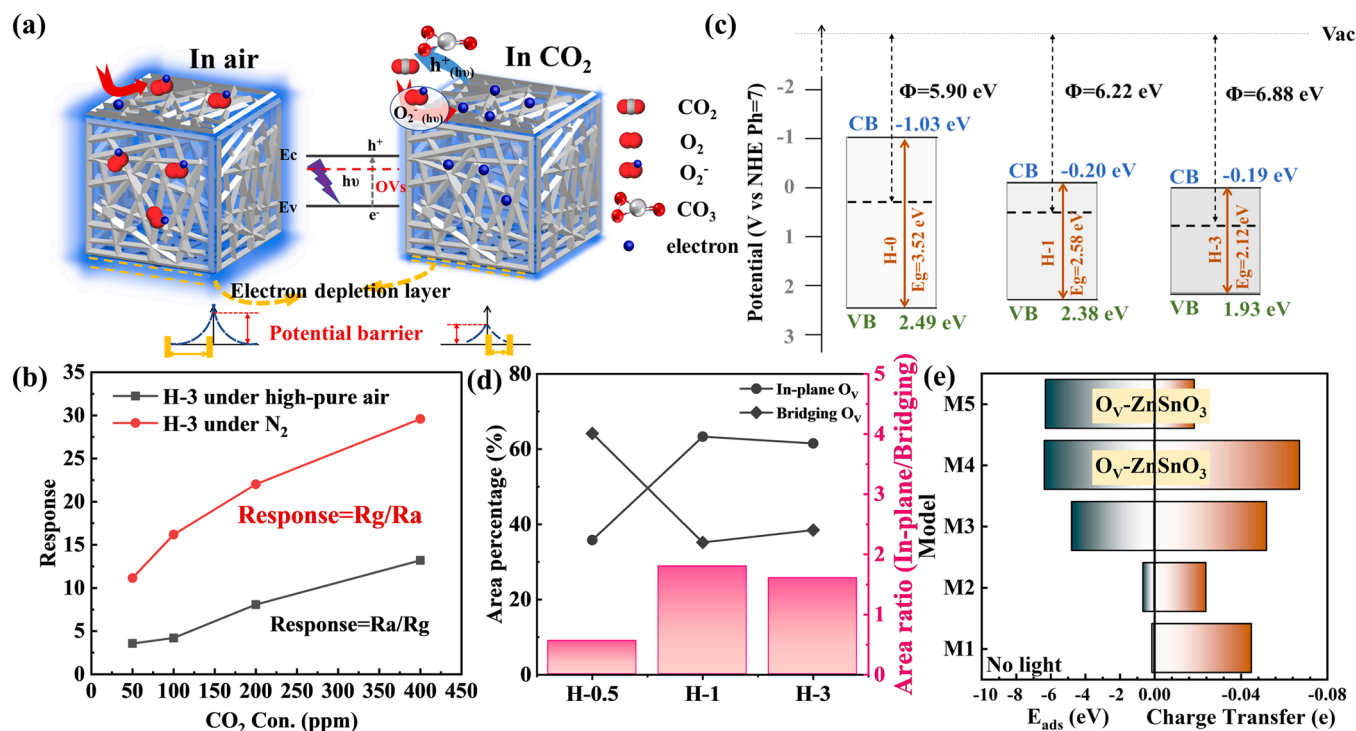


Fig. 6. (a) Schematic of the sensing process of ZnSnO₃-NCs exposed to air and CO₂ gas. (b) Response characteristics of H-3 sensor under high pure air and nitrogen atmosphere. (c) Band alignment of H-0, H-1 and H-3, where Vac is the vacuum energy level. (d) Area ratio analysis of in-plane O_V and bridging O_V in H-0.5, H-1 and H-3 through Gaussian fitting. (e) Calculated adsorption energies (left) and charge transfer (right) for various CO₂ adsorption models.

ionization energy. DFT calculations based on the model of ZnSnO₃ were performed as shown in Fig. S19, which presented that O_V created new defect level in the band gap for facilitating the excitation and migration of electrons and further narrowing the band gap. The increased density of states (DOS) at the edge of the CB observed in Ov-ZnSnO₃ indicated the reinforced migration of photogenerated charges (Fig. S17f). The VB maximum of Ov-ZnSnO₃ was primarily composed of O-p orbital while the CB minimum was the construction of hybrid orbitals of Zn-s and Sn-s, demonstrating that the photoexcited electrons may emanate from the O-p orbital and then be excited about the hybrid orbitals of Zn-s and Sn-s (Fig. S18). Furthermore, red shifts of absorption edges of the Ov-ZnSnO₃ were observed (Fig. S21a), according with the UV-vis absorption spectra of synthesized samples (Fig. 4a), which implied that the introduction of O_V caused the narrowing of the bandgap. ZnSnO₃ theoretically can only respond to UV light due to its intrinsic wide bandgap (~ 3.7 eV), but the narrowing of the bandgap decreases the threshold of excited electron transition energy, extending the absorption of light into the visible region, thus conducting to the improvement of gas sensing performance under visible light. As shown in Fig. 6c and Fig. S17a-c, the band structure of different samples was confirmed through VB-XPS method according to the empirical formula (Equation (S10)-(S12)). The VB maximum of H-1 and H-3 were found to show a distinct up-shift compared to that of pure ZnSnO₃, resulting from the homogeneous O_V confined in samples and the shallow O_V states partly overlapping with VB accompanied by an increased VB width with narrowed bandgaps, which signified relatively high mobility of holes generated and efficient photoinduced electron-hole pairs transfer and separation. Notably, the work function of materials was significantly enhanced after O_V introduction, among which H-3 showed the highest value, which is consistent with DFT calculation (Fig. S17d and S17e). This phenomenon is likely due to the transformation of materials' morphology from nanorods to nanosheets with the increase of H₂ treatment time as shown in Fig. S6f, and the differences in electronic band structures between nanorods and nanosheets lead to the construction of homojunction. In the homojunction materials, the band bending correction is accompanied by the

formation of interface dipole barrier and the change of work function, resulting from the defect-states (e.g. O_V) content increasing in one and decreasing in another. Moreover, the internal electric field promotes the segregation and transition of electrons and holes for enhancing gas sensing performance [56]. Besides, the impact of in-plane O_V (shallow donor states) and bridging O_V (deep states) of Ov-ZnSnO₃ on RT CO₂ sensing has been studied as shown in Fig. 6d and Fig. S20. In the case of H-1 and H-3, the ratio between total area of 2.38 (peak II) and 2.17 eV (peak III) corresponding to in-plane O_V and total area of 1.86 (peak IV) related to bridging O_V are 1.799 and 1.602 respectively through Gaussian fitting of PL peak (Fig. 3f). While the ratio between total area of 2.17 eV (peak I) and total area of 2.03 and 1.86 eV (peak II and peak III) is 0.558 for H-0.5. Combined with the result of gas sensing test, the strong presence of in-plane O_V over bridging O_V plays a key role in detecting CO₂ at low operation temperature, which is consistent with the results of previous studies on SnO₂ [57]. It has been discovered that bridging O_V can strongly bond oxygen species which is active at high operation temperature [56].

The contribution of in-plane O_V sites and CO₂ adsorption sites was investigated through DFT calculation. As shown in Fig. S19b, no orbital mixing and obvious structural changes occur between CO₂ and ZnSnO₃ below Fermi level, indicating that no new bond was established before and after CO₂ adsorption in these systems. Besides, the adsorption of CO₂ molecules on a clean ZnSnO₃ (001) surface was studied, and the adsorption energy (E_{ads}) and charge transfer capacity of five different structures were given in Fig. 6e. The fact that all the adsorption energies were negative suggested that these adsorption processes were spontaneous and exothermic. The relatively high absolute values of E_{ads} in M4 structures (O_V introduced, Fig. S22) demonstrated that the model was more stable and its adsorption reaction was more likely to proceed, which also proved that CO₂ molecule was tightly bound to the surface accompanied by a macroscopically prolonged recovery time (consistent with Fig. 5c).

4. Conclusion

In summary, three-dimensional ZnSnO₃ nanocubes with fine-tuned O_V were synthesized through a two-step approach comprising of hydrothermal reaction and H₂ annealing treatment. When H₂ treatment time reached 3 h, surface morphology change started to take place so that nanosheets and nanocubes coexisted. The optimal combination of high response and fast response time was obtained for H-3, which proved high performance with the combination of low LOD (3.05 ppm), outstanding response (3.594%/ppm), and short τ_{res} (16.814 s). In the future, new modification methods are anticipated to be applied in ZnSnO₃ for achieving more precise defects regulation, adapting it to be further utilized in smart farms, intelligent atmospheric monitoring equipment and other precise detection fields.

CRediT authorship contribution statement

Chao Zhang: Conceptualization, Writing – review & editing, Supervision, Funding acquisition. **Kewei Liu:** Conceptualization, Methodology, Investigation, Formal analysis, Writing – original draft. **Zichen Zheng:** Investigation, Writing – review & editing. **Marc Debliquy:** Formal analysis, Writing – review & editing, Resources, Supervision.

Declaration of Competing Interest

The authors declare that they have no known competing financial interests or personal relationships that could have appeared to influence the work reported in this paper.

Data availability

Data will be made available on request.

Acknowledgments

This work is supported by the Outstanding Youth Foundation of Jiangsu Province of China under Grant No. BK20211548, the National Natural Science Foundation of China under Grant No. 51872254, the Graduate Research Innovation Program of Jiangsu Province of China under Grant No. KYCX22_3494 and the Yangzhou City-Yangzhou University Cooperation Foundation under Grant No. YZ2021153.

Appendix A. Supporting information

Supplementary data associated with this article can be found in the online version at [doi:10.1016/j.snb.2023.133628](https://doi.org/10.1016/j.snb.2023.133628).

References

- [1] K. Caldeira, A.K. Jain, M.I. Hoffert, Climate sensitivity uncertainty and the need for energy without CO₂ emission, *Science* 299 (2003) 2052–2054, <https://doi.org/10.1126/science.1078938>.
- [2] J.C. Pales, C.D. Keeling, The concentration of atmospheric carbon dioxide in Hawaii, *J. Geophys. Res.* 70 (1965) 6053–6076, <https://doi.org/10.1029/JZ070i024p06053>.
- [3] M. MJ, CO₂ Records, <https://www.co2.earth/co2-records>.
- [4] A. Gutierrez-Ortega, R. Nomen, J. Sempere, J.B. Parra, M.A. Montes-Morán, R. Gonzalez-Olmos, A fast methodology to rank adsorbents for CO₂ capture with temperature swing adsorption, *Chem. Eng. J.* 435 (2022), 134703, <https://doi.org/10.1016/j.cej.2022.134703>.
- [5] Y.-M. Gu, H.-F. Qi, S. Qadir, T.-J. Sun, R. Wei, S.-S. Zhao, X.-W. Liu, Z. Lai, S.-D. Wang, A two-dimensional stacked metal-organic framework for ultra highly-efficient CO₂ sieving, *Chem. Eng. J.* 449 (2022), 137768, <https://doi.org/10.1016/j.cej.2022.137768>.
- [6] A. Gheorghie, O. Lugier, B. Ye, S. Tanase, Metal-organic framework based systems for CO₂ sensing, *J. Mater. Chem. C* 9 (2021) 16132–16142, <https://doi.org/10.1039/d1tc02249k>.
- [7] A. Molina, V. Escobar-Barrios, J. Oliva, A review on hybrid and flexible CO₂ gas sensors, *Synth. Met.* 270 (2020), 116602, <https://doi.org/10.1016/j.synthmet.2020.116602>.
- [8] P. Puligundla, J. Jung, S. Ko, Carbon dioxide sensors for intelligent food packaging applications, *Food Control* 25 (2012) 328–333, <https://doi.org/10.1016/j.foodcont.2011.10.043>.
- [9] X. Yang, D. Wang, Y. Tao, M. Shen, W. Wei, C. Cai, C. Ding, J. Li, L. Song, B. Yin, C. Zhu, Effects of elevated CO₂ on the Cd uptake by rice in Cd-contaminated paddy soils, *J. Hazard. Mater.* 442 (2023), 130140, <https://doi.org/10.1016/j.jhazmat.2022.130140>.
- [10] C. Zhang, K. Xu, K. Liu, J. Xu, Z. Zheng, Metal oxide resistive sensors for carbon dioxide detection, *Coord. Chem. Rev.* 472 (2022), <http://doi.org/10.1016/j.ccr.2022.214758>.
- [11] D. Hasan, C. Lee, Hybrid metamaterial absorber platform for sensing of CO₂ gas at Mid-IR, *Adv. Sci.* 5 (2018) 1700581, <https://doi.org/10.1002/adv.201700581>.
- [12] M.A. Wahab, J. Na, M.K. Masud, M.S.A. Hossain, A.A. Allothman, A. Abdala, Nanoporous carbon nitride with a high content of inbuilt N site for the CO₂ capture, *J. Hazard. Mater.* 408 (2021), 124843, <https://doi.org/10.1016/j.jhazmat.2020.124843>.
- [13] V.F.D. Martins, C.V. Miguel, J.C. Gonçalves, A.E. Rodrigues, L.M. Madeira, Modeling of a cyclic sorption-desorption unit for continuous high temperature CO₂ capture from flue gas, *Chem. Eng. J.* 434 (2022), 134704, <https://doi.org/10.1016/j.cej.2022.134704>.
- [14] Y.J. Jeong, C. Balamurugan, D.W. Lee, Enhanced CO₂ gas-sensing performance of ZnO nanopowder by La loaded during simple hydrothermal method, *Sens. Actuators B* 229 (2016) 288–296, <https://doi.org/10.1016/j.snb.2015.11.093>.
- [15] D. Wang, Y. Chen, Z. Liu, L. Li, C. Shi, H. Qin, J. Hu, CO₂-sensing properties and mechanism of nano-SnO₂ thick-film sensor, *Sens. Actuators B* 227 (2016) 73–84, <https://doi.org/10.1016/j.snb.2015.12.025>.
- [16] S. Joshi, C.B.R. Kumar, L.A. Jones, E.L.H. Mayes, S.J. Ippolito, M.V. Sunkara, Modulating interleaved ZnO assembly with CuO nanoleaves for multifunctional performance: perdurable CO₂ gas sensor and visible light catalyst, *Inorg. Chem. Front.* 4 (2017) 1848–1861, <https://doi.org/10.1039/c7qi00474e>.
- [17] A.A. Yadav, A.C. Lokhande, J.H. Kim, C.D. Lokhande, Improvement in CO₂ sensing characteristics using Pd nanoparticles decorated La₂O₃ thin films, *J. Ind. Eng. Chem.* 49 (2017) 76–81, <https://doi.org/10.1016/j.jiec.2017.01.009>.
- [18] N. Rajesh, J.C. Kannan, T. Krishnakumar, A. Bonavita, S.G. Leonardi, G. Neri, Microwave irradiated Sn-substituted CdO nanostructures for enhanced CO₂ sensing, *Ceram. Int.* 41 (2015) 14766–14772, <https://doi.org/10.1016/j.ceramint.2015.07.208>.
- [19] D. Ding, W. Lu, Y. Xiong, X. Pan, J. Zhang, C. Ling, Y. Du, Q. Xue, Facile synthesis of La₂O₂CO₃ nanoparticle films and Its CO₂ sensing properties and mechanisms, *Appl. Surf. Sci.* 426 (2017) 725–733, <https://doi.org/10.1016/j.apsusc.2017.07.126>.
- [20] N. Sahiner, Conductive polymer containing graphene aerogel composites as sensor for CO₂, *Polym. Compos.* 40 (2019) E1208–E1218, <https://doi.org/10.1002/pc.24947>.
- [21] Y. Xiong, Q. Xue, C. Ling, W. Lu, D. Ding, L. Zhu, X. Li, Effective CO₂ detection based on LaOCl-doped SnO₂ nanofibers: insight into the role of oxygen in carrier gas, *Sens. Actuators B* 241 (2017) 725–734, <https://doi.org/10.1016/j.snb.2016.10.143>.
- [22] D. Wang, X.N. Pu, X. Yu, L.P. Bao, Y. Cheng, J.C. Xu, S.N. Han, Q.X. Ma, X.Y. Wang, Controlled preparation and gas sensitive properties of two-dimensional and cubic structure ZnSnO₃, *J. Colloid Interface Sci.* 608 (2022) 1074–1085, <https://doi.org/10.1016/j.jcis.2021.09.167>.
- [23] S.D. Sun, S.H. Liang, Morphological zinc stannate: synthesis, fundamental properties and applications, *J. Mater. Chem. A* 5 (2017) 20534–20560, <https://doi.org/10.1039/c7ta06221d>.
- [24] C.X. Sun, J.K. Shao, Z.Y. Wang, H.Y. Liu, Z.H. Li, H. Zhang, T.Y. Bai, Y.W. Sun, L. L. Guo, G.F. Pan, X.L. Yang, CuO-sensitized amorphous ZnSnO₃ hollow-sunlike cubes for highly sensitive and selective H₂S gas sensors, *Sens. Actuators B* 362 (2022), <https://doi.org/10.1016/j.snb.2022.131799>.
- [25] B.S. Sa, C.A. Zito, T.M. Perfecto, D.P. Volanti, Porous ZnSnO₃ nanocubes as a triethylamine sensor, *Sens. Actuators B* 338 (2021), <https://doi.org/10.1016/j.snb.2021.129869>.
- [26] Z. Sima, P. Song, Y.L. Ding, Z.C. Lu, Q. Wang, ZnSnO₃ nanocubes/Ti₃C₂T_x MXene composites for enhanced formaldehyde gas sensing properties at room temperature, *Appl. Surf. Sci.* 598 (2022), 153861, <https://doi.org/10.1016/j.apsusc.2022.153861>.
- [27] J.T. Zhang, X.H. Jia, D.D. Lian, J. Yang, S.Z. Wang, Y. Li, H.J. Song, Enhanced selective acetone gas sensing performance by fabricating ZnSnO₃/SnO₂ concave microcube, *Appl. Surf. Sci.* 542 (2021), <https://doi.org/10.1016/j.apsusc.2020.148555>.
- [28] X.Y. Wang, H. Fu, Z.N. Qi, T. Tao, B.X. Leng, W. Xu, J.J. Ma, M.M. Wang, Significant improvement of ethanol sensitivity at low temperature for ZnSnO₃ nano-particles: co-decoration of nano-TiO₂/CeO₂ and increase of UV intensity, *Sens. Actuators B* 323 (2020), <https://doi.org/10.1016/j.snb.2020.128665>.
- [29] G.Q. Feng, Y.H. Che, C.W. Song, J.K. Xiao, X.F. Fan, S. Sun, G.H. Huang, Y.C. Ma, Morphology-controlled synthesis of ZnSnO₃ hollow spheres and their n-butanol gas-sensing performance, *Ceram. Int.* 47 (2021) 2471–2482, <https://doi.org/10.1016/j.ceramint.2020.09.090>.
- [30] Y.Y. Yin, Y.B. Shen, P.F. Zhou, R. Lu, A. Li, S.K. Zhao, W.G. Liu, D.Z. Wei, K.F. Wei, Fabrication, characterization and n-propanol sensing properties of perovskite-type ZnSnO₃ nanospheres based gas sensor, *Appl. Surf. Sci.* 509 (2020), <https://doi.org/10.1016/j.apsusc.2020.145335>.
- [31] K. Liu, Z. Zheng, M. Debliquy, C. Zhang, Highly-sensitive volatile organic compounds evaluation by three-dimensional ZnFe₂O₄/ZnSnO₃ heterostructures and their predictive grain quality monitoring, *Chem. Eng. J.* (2023), 139824, <https://doi.org/10.1016/j.cej.2022.139824>.

- [32] C.M. Hung, H.V. Phuong, V.V. Thinh, L.T. Hong, N.T. Thang, N.H. Hanh, N. Q. Dich, N.V. Duy, N.V. Hieu, N.D. Hoa, Au doped ZnO/SnO₂ composite nanofibers for enhanced H₂S gas sensing performance, *Sens. Actuators A* 317 (2021), 112454, <https://doi.org/10.1016/j.sna.2020.112454>.
- [33] S. Dabbabi, T.B. Nasr, A. Madouri, A. Cavanna, A. Garcia-Loureiro, N. Kamoun, Fabrication and characterization of sensitive room temperature NO₂ gas sensor based on ZnSnO₃ thin film, *Phys. Status Solidi A* 216 (2019) 1900205, <https://doi.org/10.1002/pssa.201900205>.
- [34] T. Shujah, M. Ikram, A.R. Butt, S.G. Hussain, M.K. Shahzad, Q. Zafar, S. Ali, Growth of zinc oxide and zinc stannate nanostructured thin films for carbon monoxide sensing application, *Nanosci. Nanotech. Lett.* 11 (2019) 1050–1059, <https://doi.org/10.1166/nnl.2019.2987>.
- [35] K. Liu, Z. Zheng, J. Xu, C. Zhang, Enhanced visible light-excited ZnSnO₃ for room temperature ppm-level CO₂ detection, *J. Alloy. Compd.* 907 (2022), 164440, <https://doi.org/10.1016/j.jallcom.2022.164440>.
- [36] X.Y. Wang, H. Li, X.T. Zhu, M.Z. Xia, T. Tao, B.X. Leng, W. Xu, Improving ethanol sensitivity of ZnSnO₃ sensor at low temperature with multi-measures: Mg doping, nano-TiO₂ decoration and UV radiation, *Sens. Actuators B* 297 (2019), <https://doi.org/10.1016/j.snb.2019.126745>.
- [37] Y. Yan, J.Y. Liu, H.S. Zhang, D.L. Song, J.Q. Li, P.P. Yang, M.L. Zhang, J. Wang, One-pot synthesis of cubic ZnSnO₃/ZnO heterostructure composite and enhanced gas-sensing performance, *J. Alloy. Compd.* 780 (2019) 193–201, <https://doi.org/10.1016/j.jallcom.2018.11.310>.
- [38] L.Y. Du, H.M. Sun, Facile fabrication and enhanced gas sensing properties of ZnSnO₃/NiO heterostructures, *J. Mater. Sci. Mater. Electron* 33 (2022) 15734–15741, <https://doi.org/10.1007/s10854-022-08475-4>.
- [39] Z.C. Zheng, K.W. Liu, K.C. Xu, C. Zhang, Investigation on microstructure and nonanal sensing properties of hierarchical Sb₂WO₆ microspheres, *Ceram. Int.* 48 (2022) 30249–30259, <https://doi.org/10.1016/j.ceramint.2022.06.298>.
- [40] Z.Y. Wang, J.Y. Miao, H.X. Zhang, D. Wang, J.B. Sun, Hollow cubic ZnSnO₃ with abundant oxygen vacancies for H₂S gas sensing, *J. Hazard. Mater.* 391 (2020), <https://doi.org/10.1016/j.jhazmat.2020.122226>.
- [41] G. Bruno, M.M. Giangregorio, G. Malandrino, P. Capezzuto, I.L. Fragalà, M. Losurdo, Is there a ZnO face stable to atomic hydrogen, *Adv. Mater.* 21 (2009) 1700–1706, <https://doi.org/10.1002/adma.200802579>.
- [42] V. Gurylev, T.P. Perng, Defect engineering of ZnO: review on oxygen and zinc vacancies, *J. Eur. Ceram. Soc.* 41 (2021) 4977–4996, <https://doi.org/10.1016/j.jeurceramsoc.2021.03.031>.
- [43] Q. Zhu, C.S. Xie, H.Y. Li, C.Q. Yang, S.P. Zhang, D.W. Zeng, Selectively enhanced UV and NIR photoluminescence from a degenerate ZnO nanorod array film, *J. Mater. Chem. C* 2 (2014) 4566–4580, <https://doi.org/10.1039/c4tc00011k>.
- [44] J.J. Wu, H.I. Wen, C.H. Tseng, S.C. Liu, Well-aligned ZnO nanorods via hydrogen treatment of ZnO films, *Adv. Funct. Mater.* 14 (2004) 806–810, <https://doi.org/10.1002/adfm.200305092>.
- [45] C. Zhang, Y. Li, G.F. Liu, K.W. Liu, K.D. Wu, Room temperature NO₂ sensing properties of ZnO_{1- α} coating prepared by hydrogen reduction method, *Ceram. Int.* 47 (2021) 29873–29880, <https://doi.org/10.1016/j.ceramint.2021.07.160>.
- [46] C. Zhang, G.F. Liu, X. Geng, K.D. Wu, M. Debligny, Metal oxide semiconductors with highly concentrated oxygen vacancies for gas sensing materials: a review, *Sens. Actuators A* 309 (2020), <https://doi.org/10.1016/j.sna.2020.112026>.
- [47] J. Lee, Y. Choi, B.J. Park, J.W. Han, H.-S. Lee, J.H. Park, W. Lee, Precise control of surface oxygen vacancies in ZnO nanoparticles for extremely high acetone sensing response, *J. Adv. Ceram.* 11 (2022) 769–783, <https://doi.org/10.1007/s40145-022-0570-x>.
- [48] N. Van Hoang, C.M. Hung, N.D. Hoa, N. Van Duy, N. Van Hieu, Facile on-chip electrospinning of ZnFe₂O₄ nanofiber sensors with excellent sensing performance to H₂S down ppb level, *J. Hazard. Mater.* 360 (2018) 6–16, <https://doi.org/10.1016/j.jhazmat.2018.07.084>.
- [49] A.V. Moholkar, S.M. Pawar, K.Y. Rajpure, P.S. Patil, C.H. Bhosale, Properties of highly oriented spray-deposited fluorine-doped tin oxide thin films on glass substrates of different thickness, *J. Phys. Chem. Solids* 68 (2007) 1981–1988, <https://doi.org/10.1016/j.jpcs.2007.06.024>.
- [50] A.K. Gangwar, R. Godiwal, J. Jaiswal, V. Baloria, P. Pal, G. Gupta, P. Singh, Magnetron configurations dependent surface properties of SnO₂ thin films deposited by sputtering process, *Vacuum* 177 (2020), 109353, <https://doi.org/10.1016/j.vacuum.2020.109353>.
- [51] O. Dimitrov, I. Stambolova, T. Babeva, K. Lazarova, G. Avdeev, M. Shipochka, R. Mladenova, S. Simeonova, High intensity orange-red emission of chemically deposited Sm³⁺-doped ZrO₂ thin films - beneficial effects of host and dopant, *J. Mater. Res. Technol.* 18 (2022) 3026–3034, <https://doi.org/10.1016/j.jmrt.2022.04.013>.
- [52] M.S. Yao, W.X. Tang, G.E. Wang, B. Nath, G. Xu, MOF thin film-coated metal oxide nanowire array: significantly improved chemiresistor sensor performance, *Adv. Mater.* 28 (2016) 5229–5234, <https://doi.org/10.1002/adma.201506457>.
- [53] T. Bhowmick, A. Ghosh, S. Nag, S.B. Majumder, Sensitive and selective CO₂ gas sensor based on CuO/ZnO bilayer thin-film architecture, *J. Alloy. Compd.* 903 (2022), 163871, <https://doi.org/10.1016/j.jallcom.2022.163871>.
- [54] S. Kanaparthi, S.G. Singh, Chemiresistive sensor based on zinc oxide nanoflakes for CO₂ detection, *ACS Appl. Nano Mater.* 2 (2019) 700–706, <https://doi.org/10.1021/acsanm.8b01763>.
- [55] M. Al-Hashem, S. Akbar, P. Morris, Role of oxygen vacancies in nanostructured metal-oxide gas sensors: a review, *Sens. Actuators B* 301 (2019), 126845, <https://doi.org/10.1016/j.snb.2019.126845>.
- [56] M. Epifani, J.D. Prades, E. Comini, E. Pellicer, M. Avella, P. Siciliano, G. Faglia, A. Cirera, R. Scotti, F. Morazzoni, J.R. Morante, The role of surface oxygen vacancies in the NO₂ sensing properties of SnO₂ nanocrystals, *J. Mater. Chem. C* 112 (2008) 19540–19546, <https://doi.org/10.1021/jp804916g>.
- [57] L.Z. Liu, J.Q. Xu, X.L. Wu, T.H. Li, J.C. Shen, P.K. Chu, Optical identification of oxygen vacancy types in SnO₂ nanocrystals, *Appl. Phys. Lett.* 102 (2013), 031916, <https://doi.org/10.1063/1.4789538>.

Chao Zhang received a B.S. degree from the Chongqing University (China) in 2003 and a joint Ph.D. degree from Technology University of Belfort-Montbéliard (France) and Xi'an Jiaotong University (China) in June 2008. From September 2007 to January 2009, he worked as a teaching-research assistant in Technology University of Belfort-Montbéliard. Since Feb 2009, he is postdoctoral researcher, and then a senior researcher in Materials Science Department of engineering School of University of Mons (Belgium). In 2014, he joined Yangzhou University (China) as professor where he is leading a research group on thermal spray coatings and gas sensors. Since August 2016, he is Vice Dean in charge of research in College of Mechanical Engineering. His research interests include thermal-sprayed techniques and coatings, especially gas sensing and wear-resistant coatings.

Kewei Liu received her B.S. degree in 2019 at Yangzhou University (China). She is currently pursuing her joint Ph.D degree at Yangzhou University and University of Mons. She takes interests in metal oxides based gas sensors for detecting pollutant gases.

Zichen Zheng received his B.S. degree in 2020 at Hefei University of Technology (China). He is currently pursuing his Ph.D degree at Yangzhou University (China). He takes interests in smart materials for high-performance gas sensors working at room temperature.

Marc Debligny received his Ph.D. at Faculty of Engineering in Mons (Belgium) in 1999 in the field of organic semiconductors for fire detection. He joined the Sochinor Company in 2000. He left in 2003 for joining Materia Nova. He was responsible for the research activities in the field of gas sensors. Since October 2008, he joined the Material Science Department of Faculty of Engineering of University of Mons and worked as a team leader of semiconductor and sensor group. He was promoted as associate professor in September 2013. His main research interest is smart coatings for chemical detection. He is also co-founder of the spin off company B-Sens specialized in optical fiber sensors.